Chapter 6

Synthesis and Characterisation of $Sr_2Mn_{1-x}Nb_xO_4$

Part of this chapter is published as ‘Gurudeo Nirala, Tarun Katheriya, Dharmendra Yadav, Shukdev Pandey, and Shail Upadhyay; Effect of Nb doping on epsilon negative behaviour of Sr_2MnO_4; *J. Mater. Sci.* **57**, 15862-15875 (2022).’

Synthesis and Characterisation of $Sr_2Mn_{1-x}Nb_xO_4$

6.1 Introduction

In electronic devices, the miniaturized and highly integrated circuits require the contributing dielectrics to possess high dielectric permittivity and low loss. The high positive dielectric constant is attributed to the localized charge carriers or ions of the materials [267]. The dielectric properties of materials showing positive permittivity have been investigated extensively. Recently, materials with negative permittivity or/and negative permeability have attracted attention of the researchers due to their novel applications, such as electromagnetic shielding [119], capacitors [222], transistors [223], antennas [224], inductor design, and for other electronic devices. The negative permittivity is common in metals (or semiconductors) due to the plasmonic oscillations of free electrons. But the plasma frequencies of metals are mainly observed at ultraviolet frequencies, several orders higher than that of the radio frequencies [236]. To lower the plasmonic frequencies of the metals, new materials known as metamaterials were fabricated. The negative permittivity of metamaterials is tailorable and depends on artificial geometrical dimensions and configurations of periodic metallic wires and rings [102,118,225]. An extensive literature survey has demonstrated that negative permittivity can also be realized in composites with functional metal fillers randomly dispersed in an insulator matrix [109,112,250,251].

According to Drude's model, the plasma frequency decreases with the decreasing charge carrier concentration/density. Therefore, efforts have been made to lower the plasmonic oscillation in the radio frequency region by diluting carrier concentration. Negative permittivity in radio frequencies range has been realized in many polymer matrices [108,229–233,268] and ceramic matrix composites [137,234]. In these two classes of composites the insulating polymers or ceramics act as matrices and play an important role in diluting electrons concentration of metals or carbon materials. Thus, average electron concentration can be controlled by the contents of conductors to achieve a negative permittivity at frequencies lower than ultraviolet frequencies [229,234].

Once it was confirmed that the negative permittivity property hinges on the concentration of carriers in materials [236], efforts were made to realize negative permittivity in single-phase homogeneous materials because by compositional modification charge carrier concentration can be optimized. Negative permittivity at radio frequencies has been observed in Sb doped SnO_2 [261], Sn doped In_2O_3 [236], and Sr doped $LaMnO_3$ [259,263]. In our recent studies, we have been able to realize negative permittivity in the Sr_2MnO_4 system [269].

The Sr_2MnO_4 is isostructural to the K_2NiF_4, crystallized with a tetragonal unit cell in the space group I4/mmm [238]. The oxides of the K_2NiF_4-type belong to the n=1 member of the Ruddlesden–Popper (RP) phases of the general formula $A_{n+1}B_nO_{3n+1}$. The Sr_2MnO_4 comprises perovskite (ABO3) layers separated by rock-salt layer (AO) along the c-axis [179]. The studied compositions of the system $Sr_2Mn_{1-x}Sn_xO_4$ have exhibited negative permittivity above room temperature, different for different compositions [269]. The lowest temperature was observed for $Sr_2Mn_{0.7}Sn_{0.3}O_4$ which was 220 °C, well above the room temperature. As most of the devices work at room temperature hence, materials showing negative permittivity at room temperature are required. In this system, it is observed that the lowest temperature at which negative permittivity is observed depends on DC conductivity i.e., on charge carrier concentration. By choosing a suitable donor or acceptor dopants for the Sr and Mn sites, DC conductivity/charge carrier concentration of Sr_2MnO_4 can be tailored, and hence the lowest temperature at which negative permittivity is observed is achievable. Intending to reduce critical temperature, we have chosen donor Nb for the Mn site of Sr_2MnO_4. A few compositions of the system $Sr_2Mn_{1-x}Nb_xO_4$ (x = 0.1, 0.2, 0.3, 0.4 & 0.5) have been synthesized by solid-state reaction method. In this work, the effect of Nb substitution at Mn site on phase formation, microstructure, and dielectric properties have been investigated. The dielectric and electrical properties of synthesized compositions were investigated by measuring real (Z') and imaginary (Z") components of the impedance, Z, in the temperature range 30-600 °C and in the frequency range 20 Hz - 2 MHz.

6.2 Experimental

In this work, Nb substituted $Sr_2Mn_{1-x}Nb_xO_4$ (x = 0.1, 0.2, 0.3, 0.4 & 0.5) has been prepared using conventional solid-state reaction route. The starting compounds $SrCO_3$ (Sigma-Aldrich, purity ≥ 99.9%), MnO_2 (Sigma-Aldrich, purity ≥ 99%), and Nb_2O_5 (Alfa Aesar, purity ≥ 99.9%) were taken in the stoichiometric ratio and mixed in an Agate Mortar and Pestle by hand using acetone as mixing medium. The mixtures were then calcined for 12 hours at 1200 °C in a high-temperature furnace (HTRH-70/150, Carbolite Gero, UK). Calcined powders were ground in an agate mortar and recalcined for 24 hours at 1500 °C with an intermediate grinding. For microstructure, XPS, and electrical measurements, the pellets with a diameter of 11-12 mm and a thickness of 2-3 mm were prepared using a hydraulic press by applying the pressure of 5 kN. Green pellets were sintered in a muffle furnace at 1500 °C for 12 hours. For stabilizing $Sr_2Mn_{0.9}Nb_{0.1}O_4$ and $Sr_2Mn_{0.8}Nb_{0.2}O_4$ compositions in a single tetragonal phase with I4/mmm space group pellets were quenched in air to room temperature from 1500 °C. Other compositions $Sr_2Mn_{0.7}Nb_{0.3}O_4$, $Sr_2Mn_{0.6}Nb_{0.4}O_4$, and $Sr_2Mn_{0.5}Nb_{0.5}O_4$ didn't require a quenching process to stabilize in a single tetragonal phase with I4/mmm space, therefore, pellets of these compositions were cooled to room temperature with a normal cooling rate of 4 °C/min. For convenience, in succeeding sections samples have been addressed with a short name such as SMNb1, SMNb2, SMNb3, SMNb4, and SMNb5 for $Sr_2Mn_{0.9}Nb_{0.1}O_4$, $Sr_2Mn_{0.8}Nb_{0.2}O_4$, $Sr_2Mn_{0.7}Nb_{0.3}O_4$, $Sr_2Mn_{0.6}Nb_{0.4}O_4$, and $Sr_2Mn_{0.5}Nb_{0.5}O_4$, respectively.

The X-ray diffraction (XRD) pattern of the sintered pellets was recorded at room temperature using a diffractometer (Rigaku Miniflex II Desktop, Japan). The morphological fingerprints of fractured surfaces of the sintered pellets were recorded using a Scanning Electron Microscope (Nova Nano SEM 450, USA). For dielectric/electrical properties measurements, circular surfaces of the sintered pellets were polished using emery paper of different grades and then coated with a thin and uniform layer of high-temperature silver paste. Real (Z') and imaginary (Z'') parts of the impedance (Z) were measured as a function of the frequency (in the range of 20 Hz–2 MHz) and temperature (in the range of 30-600 ^{o}C), using an inductance-capacitance-resistance (LCR) meter (Agilent E-4980, USA). For studying the valence state of constituent elements Mn and Nb, present in bulk, the pellets' surfaces were scorched and further polished with the various grades of emery paper. Thereafter, the core spectra of these elements were obtained using an X-ray photoelectron spectrometer (Thermo Fisher Scientific K-Alpha, USA), operating at the high pressure of 5×10^{-11} Torr.

6.3 Results and Discussion

6.3.1 Phase analysis and Crystal structure

The X-ray diffraction (XRD) pattern of prepared compositions $Sr_2Mn_{1-x}Nb_xO_4$(x = 0.10, 0.20, 0.30, 0.40 and 0.50) were recorded and shown in Fig. 6.1(a). The XRD patterns were matched with the Crystallography Open Database (COD) for Sr_2MnO_4 (1008125). No distinct peaks corresponding to raw materials SrO, MnO_2, and Nb_2O_5 or expected secondary phase $Sr_7Mn_4O_{15}$ were observed in all samples. However, in samples SMNb4 and SMNb5, a distinct peak at 30.64° was observed, which corresponds to $Sr_8Nb_4O_{18}$ [270]. A systematic shift in measured peaks (highlighted in inset) corresponding to the plane (103) and (110) was observed for the samples SMNb1, SMNb2, and SMNb3. On the other hand, for the samples SMNb4 and SMNb5, no further peak shift with respect to SMNb3 was observed. The ionic radius of Nb^{5+} is 0.64 Å, higher than the ionic radius of Mn^{4+} (0.53 Å) in the same coordination number six [239]. Therefore, the observed peak shift towards lower angle side in the samples SMNb1, SMNb2, and SMNb3 indicate the replacement of Mn^{4+} ions by Nb^{5+} ions in the unit cells of Sr_2MnO_4. No peak shift with respect to SMNb3 for the samples SMNb4 and SMNb5 indicates a substitution limit or solubility limit of Nb in Sr_2MnO_4 system. It is also important to notice here that major peaks corresponding to the plane (103) and (110) of Sr_2MnO_4 system appear at the same angle for both SMNb4 and SMNb5 samples, which implies that even after increasing the content of Nb no further incorporation happens in Sr_2MnO_4 unit cells, i.e., the solubility limit is unaffected. However, the peak height (intensity) of the impurity phase is lower in the sample SMNb4 and higher in the sample SMNb5, which implies that the impurity content in SMNb4 is less than SMNb5. This also supports the above argument. These observations confirm that a higher substitution of Nb (i.e., $x > 0.30$) at Mn site in Sr_2MnO_4 system leads to the formation of new compound $Sr_8Nb_4O_{18}$ and creates an admixture of Sr_2MnO_4 and $Sr_8Nb_4O_{18}$ as a final product. We can conclude here that the samples SMNb1, SMNb2 and SMNb3 are a single-phase solid solution whereas the samples SMNb4 and SMNb5 have small amount of impurity phase of$Sr_8Nb_4O_{18}$. The amount of impurity phase increases with increasing Nb content in the solid solution $Sr_2Mn_{1-x}Nb_xO_4$.

The accurate value of the lattice parameters and conten t of impurity phase for all the samples were obtained with the help of Rietveld refinement using the FullProf Suite software package. The structural refinement was carried out by considering the tetragonal structure and space group I4/mmm for the samples SMNb1, SMNb2, and SMNb3 and for the remaining two samples SMNb4 and SMNb5 another triclinic phase having space group 1 of $Sr_8Nb_4O_{18}$ is incorporated in the refinement. The calculated XRD pattern after the final refinement is shown in Fig. 6.1(b-e). A good match between the experimentally recorded and calculated XRD patterns was seen. Value of the lattice parameter and impurity content are mentioned in Table

6.1. For comparison, the value of lattice parameters of undoped Sr_2MnO_4 was taken from the reference [238] are incorporated in Table 6.1. The variation of lattice parameters and the unit cell volume with dopant (Nb) concentration (x) is shown in Fig. 6.1(f). The lattice parameter 'a = b', has increased while 'c' remained constant with increasing Nb content (up to x = 0.30). This result has demonstrated that the unit cell has expanded only along the a- and b-axis (longitudinally), no expansion along the c-axis (transverse direction) has occurred. The unit cell expansion is consistent with the peak shift observed in the XRD pattern of the samples SMNb1, SMNb2, and SMNb3. For samples SMNb4 and SMNb5, the lattice parameters 'a = b' of tetragonal phase are marginally higher than SMNb3 which indicates marginally higher Nb incorporation, i.e., the solubility limit slightly higher than x = 0.30. The solubility limit can be calculated according to Vegard's law by extrapolating the linear increment in 'a = b' lattice parameter. The calculated solubility limit of Nb in Sr_2MnO_4 is x= 0.33 ± 0.01, shown in Fig. 6.1(f).

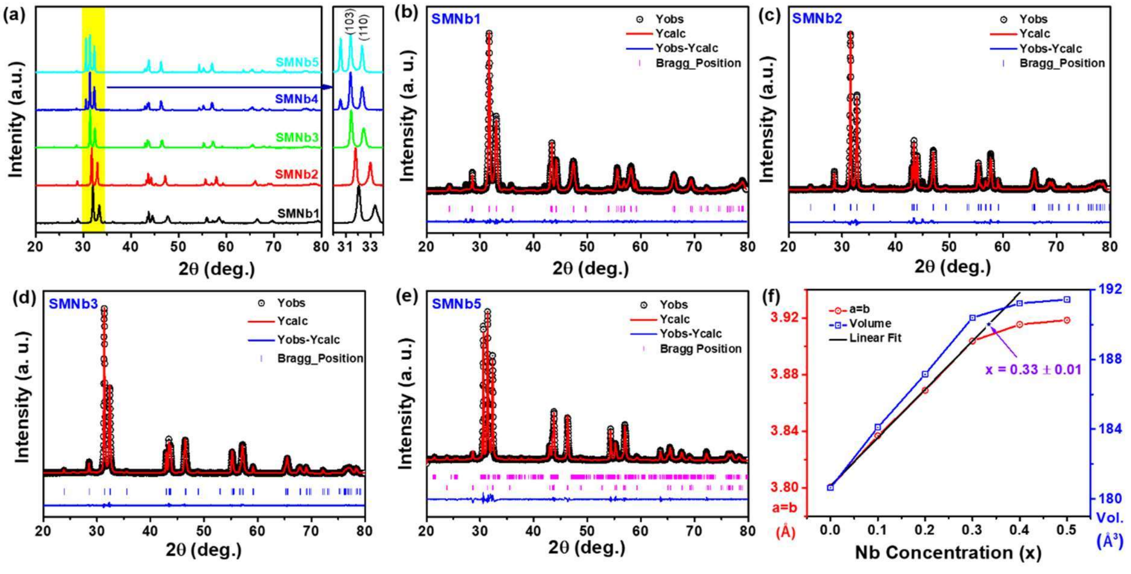

Figure 6.1. (a) Room temperature XRD pattern of the samples, (b, c, d, e) Rietveld refined XRD pattern of the samples (f) Variation of lattice parameters with Nb Concentration (x).

The tolerance factor (t) and Global instability index (GII) have been calculated to analyze the stability of prepared solid solutions. For layered perovskites, t estimates the compatibility of perovskite and rocksalt layers. While GII represents the instability of the structure and a larger GII indicates a less stable structure [240]. The equations for the calculation of the tolerance factor and Global instability index (GII) are given below:

$$t = \frac{r_{Sr} + r_O}{\sqrt{2} * ((1-x) \times r_{Mn} + x \times r_{Nb} + r_O)} \qquad (6.1)$$

where $r_{Sr}, r_{Mn}, r_{Nb}, r_O$ are the effective radii of Sr, Mn, Nb, O, respectively and x is the Nb concentration in the prepared samples. And,

$$GII = \frac{\sqrt{\sum_{i=1}^{N}\{\sum_j (S_{ij} - V_i)^2\}}}{N} \qquad (6.2)$$

where S_{ij} is the sum of the valence bonds around each ion and $V_i = \sum_j S_{ij}$. The value of S_{ij} is determined by the semi-empirical expression $S_{ij} = \exp[(R_o - R_{ij})/0.37]$, where R_o is a constant characteristic of the bond type. Calculated values of tolerance factor (t) and Global instability index (GII) are listed in Table 6.1. As Nb concentration (x) increases tolerance factor (t) decreases whereas the Global instability index (GII) first increases for x = 0.1 thereafter decreases. The Sr_2MnO_4 is stable only at temperatures higher than 1350 °C, below this temperature it decomposes into $Sr_7Mn_4O_{15}$ and SrO [165]. To stabilize Sr_2MnO_4 phase at lower temperatures approximately 30% of Mn ions should be present in Mn^{3+} state [73,241]. To achieve this goal, the synthesis of Sr_2MnO_4 has been carried out in reducing atmospheres [241–244]. In our recent studies, we had been able to stabilize Sr_2MnO_4 at room temperature by quenching from the high temperature (1500°C) to room temperature in air [238]. The donor doping of Nb can also manipulate the concentration of Mn^{3+} cations. Thus, Nb may play the same role as reducing atmosphere/ quenching are playing in stabilizing Sr_2MnO_4 phase at lower temperatures. Here it is also important to mention that, the calculated values of t and GII of Nb substituted Sr_2MnO_4 are in the range of other reported A_2BO_4 compounds [179,240,245,246].

Table 6.1. Structural parameters and reliability factors obtained by Rietveld refinement of the XRD patterns.

Sample Code		Sr_2MnO_4	SMNb1	SMNb2	SMNb3	SMNb4	SMNb5
$Sr_8Nb_4O_{18}$ fraction (%)		-	0	0	0	7.10	18.50
Tetragonal phase	a = b (Å)	3.795	3.837	3.868	3.903	3.915	3.918
	c (Å)	12.500	12.505	12.503	12.493	12.473	12.467
	Cell Volume (Å^3)	180.63	184.11	187.15	190.40	191.22	191.44
	t	0.993	0.987	0.981	0.976	0.970	0.965
	GII	0.33	0.37	0.33	0.33	0.32	0.31
Triclinic phase	a (Å)	-	-	-	-	5.846	5.844
	b (Å)	-	-	-	-	5.843	5.843
	c (Å)	-	-	-	-	14.325	14.334
	α	-	-	-	-	89.96	89.89
	β	-	-	-	-	89.87	90.00
	γ	-	-	-	-	119.93	119.95
	Cell Volume (Å^3)	-	-	-	-	424.12	424.13
R_p			4.05	12.0	6.36	11.3	10.2
R_{wp}			6.12	13.7	6.24	12.3	11.4
R_{exp}			2.26	4.57	3.49	4.91	4.88
$\chi 2$			4.32	3.82	3.20	6.27	5.45

6.3.2 Microstructural characterization

For studying the effect of Nb substitution on morphology, a scanning electron microscopy (SEM) technique was employed. The recorded SEM micrographs corresponding to the fractured surfaces of the sintered pellets are shown in Fig. 6.2. The micrographs corresponding to each composition show well-developed grains, separated by well-defined grain boundaries, a typical characteristic feature of a polycrystalline material. The micrographs of the samples SMNb1, SMNb2, and SMNb3 are homogeneous. On the other hand, for the samples SMNb4 and SMNb5, the micrographs are not homogeneous and consist of some impurities or other phase(s). As mentioned above the SMNb4 and SMNb5 have some amount of impurity phase of $Sr_8Nb_4O_{18}$, less in SMNb4 and higher in SMNb5. The noticeable change in the microstructure of SMNb5 is consistent with the XRD results.

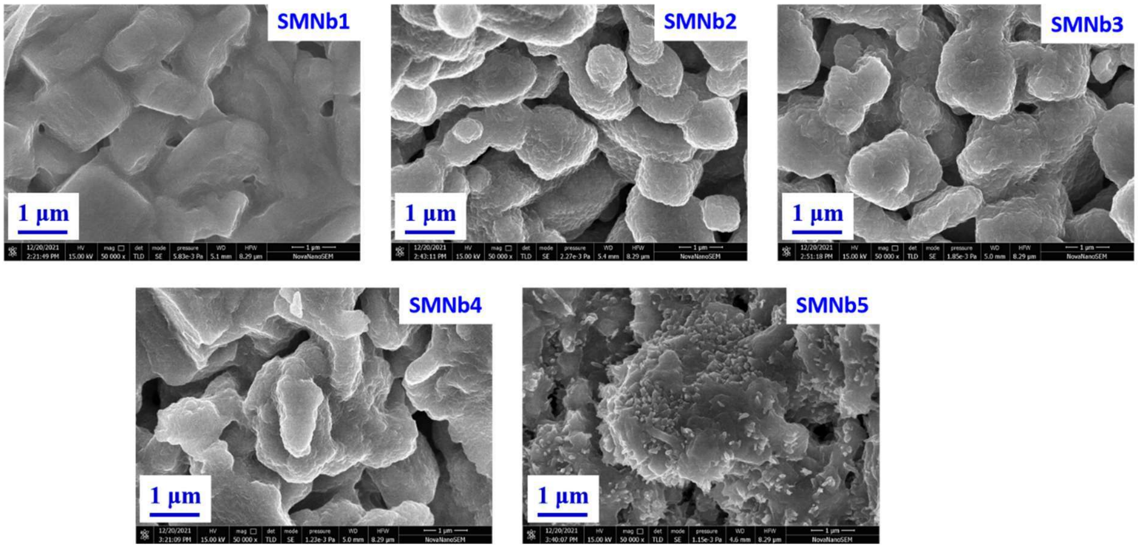

Figure 6.2. SEM images of the fractured surfaces of the sintered pellets.

6.3.3 X-Ray Photoelectron Spectroscopy Analysis

X-ray photoelectron spectroscopy (XPS) has been used to elucidate the valence state of the constituent ions (Mn and Nb). Fig. 6.3 shows the core level Mn 2p and Nb 3d spectra of the samples SMNb1, SMNb2, SMNb3, and SMNb4. All binding energies were calibrated based on the C 1s peak at 285 eV. The spectrum of Mn exhibits two primary peaks for all the samples corresponding to Mn $2p_{1/2}$ and $2p_{3/2}$ due to spin-orbit coupling [238,247]. The position of these peaks remains nearly same for all the samples. However, the broadening and asymmetry of the peaks are different for different samples. The peak corresponding to Mn $2p_{3/2}$ was deconvoluted to investigate the possible valence states. The XPS core level binding energy corresponding to different elements and their valence states are summarized in Table 6.2. Percentage (%) fractions of Mn^{3+} and Mn^{4+} are calculated from the peak area, also given in Table 6.2. It is already mentioned that these samples were prepared at 1500 °C, therefore loss of oxygen from the lattice is expected. The loss of oxygen is maximum in the samples SMNb1 and SMNb2, since these two samples are prepared by quenching process from 1500 °C to room temperature. Therefore, the time for absorbing oxygen from the atmosphere is minimal. According to defect chemistry, the loss of oxygen in Kröger–Vink notation is as follows:

$$O_o^{\times} \rightarrow V_o^{\bullet\bullet} + 2e' + \frac{1}{2}O_2(g)\uparrow \qquad (6.3)$$

The electrons released in Eqn. (6.3) may be captured by Mn^{4+} cations and reduced to Mn^{3+}. In the literature, it has been mentioned that the Sr_2MnO_4 phase can be stabilized at lower temperatures only when it contains around 30% Mn ions in Mn^{3+} state [73,241]. Reduction of Mn^{4+} state into Mn^{3+} state has been realized by synthesizing in a reducing atmosphere and quenching [238]. The donor doping of Nb in Sr_2MnO_4 at the Mn site has further reduced Mn^{4+} cation into the Mn^{3+} oxidation state, leading to an overall concentration of Mn^{3+} in all samples to around 70%.

The core spectra of Nb 3d for the samples SMNb1, SMNb2, SMNb3, and SMNb4 are also shown in Fig. 6.3. The Nb spectrum also exhibits two primary peaks for all the samples corresponding to Nb $3d_{5/2}$ and Nb $3d_{3/2}$ due to spin-orbit coupling [271,272]. These peaks are analyzed by fitting the Gaussian-Lorentzian function. The obtained XPS peak positions of Nb are also nearly same for all the samples. The exact values of binding energy for different states are also given in Table 6.2.

Table 6.2. XPS core level binding energy of Mn 2p and Nb 3d.

Elements	**Mn $2p_{1/2}$**	**Mn $2p_{3/2}$**		**Concentration of Mn^{3+}**	**Nb $3d_{3/2}$**	**Nb $3d_{5/2}$**
		Mn^{4+}	**Mn^{3+}**		**Nb^{5+}**	**Nb^{5+}**
Sample Code	**B. E. (eV)**	**B. E. (eV)**	**B. E. (eV)**	**%**	**B. E. (eV)**	**B. E. (eV)**
SMNb1	653.60	643.28	641.75	68.84	208.91	206.16
SMNb2	653.66	643.27	641.81	67.55	209.01	206.28
SMNb3	653.55	643.22	641.63	67.29	209.15	206.42
SMNb4	653.38	643.05	641.44	66.28	209.07	206.34

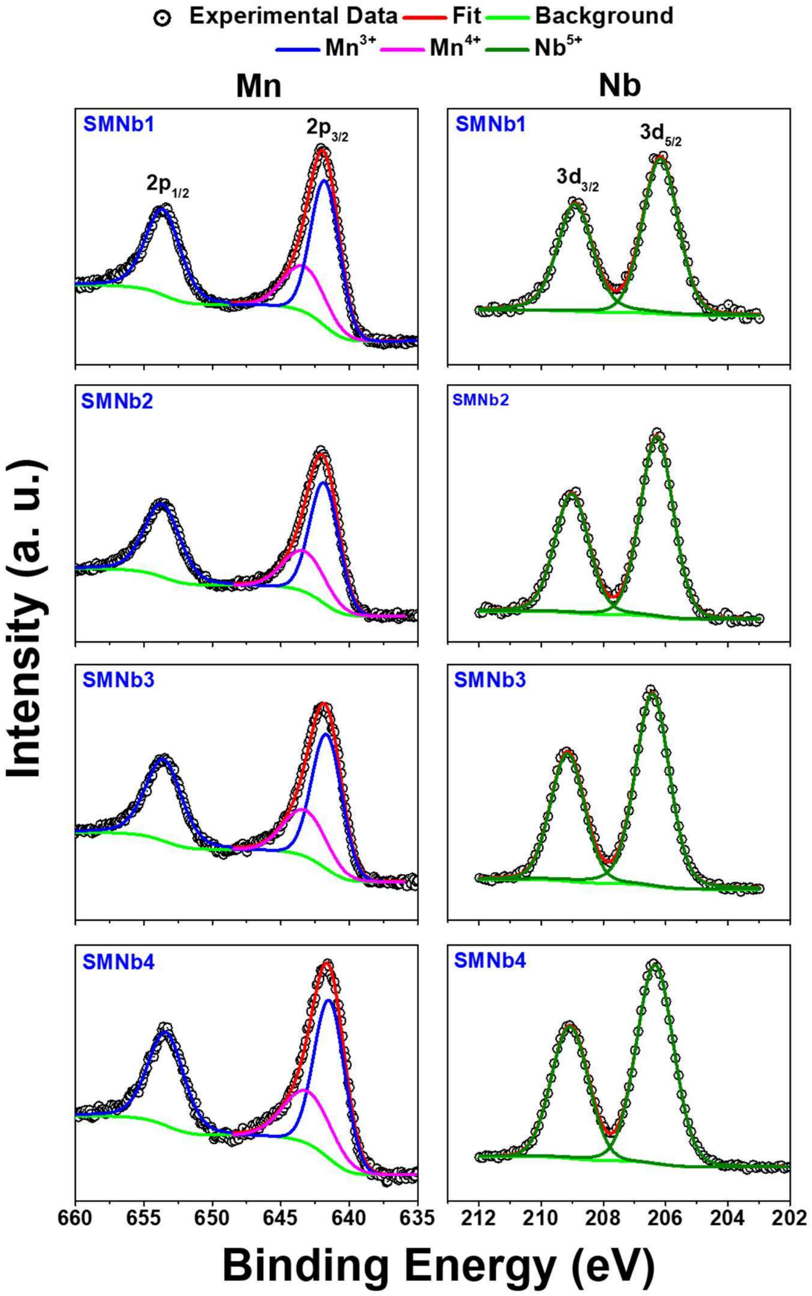

Figure 6.3. Core-level XPS spectra of Mn 2p and Nb 3d.

6.3.4 Negative Permittivity

The permittivity of the samples was calculated from measured impedance data, by the following equation:

$$\varepsilon_r^* = \frac{1}{i\omega C_0 Z^*} \qquad (6.4)$$

where, $\varepsilon_r^*(=\varepsilon_r' + i\varepsilon_r'')$ is complex relative permittivity, i is an imaginary unit ($i^2 = -1$), ω is the angular frequency of the applied signal, $C_0 = \varepsilon_0 A/d$, ε_0 = permittivity of free space (8.85×10^{-12} Fm^{-1}), A = electrode surface area, d = separation between the electrodes and $Z^*(= Z' + iZ'')$ is complex impedance. The variation of the real component of the relative permittivity, ε_r' and their respective dissipation factor,$tan\delta$ with the temperature at some representative frequencies for all samples are shown in Fig. 6.4. The ε_r' vs temperature plot and $tan\delta$ vs temperature plots for SMNb1 and SMNb2 are similar. The permittivity values and dissipation factor are negative at all measuring frequencies (20 Hz- 2 MHz) as well as at all measuring temperatures, i.e., starting from room temperature to 600 °C, however, their variations are very different. The absolute value of ε_r' increases with increasing temperature whereas $tan\delta$ decreases with increasing temperature. On the other hand, for the samples SMNb3, SMNb4 and SMNb5, the permittivity values remain almost constant and positive up to a particular temperature and begin to decrease, and become negative at higher temperatures. The dissipation factor is initially positive and increases exponentially. Thereafter it changes its sign from positive to negative and decreases exponentially, and shows a spike kind of behavior in its variation with temperature. The ε_r' and $tan\delta$ both change their sign at the same temperature. The temperature at which, ε_r' or $tan\delta$ changes sign is referred to as critical transition temperature (T_c). The value of T_c is different for different samples, 80 °C, 180 °C, and 230 °C, respectively for the samples SMNb3, SMNb4 & SMNb5. The plot of $tan\delta$ for the samples SMNb3, SMNb4 & SMNb5 above T_c is similar to the SMNb1 and SMNb2. From it, we can speculate that T_c values for samples SMNb1 and SMNb2 are below the room temperature and lower for SMNb1 than the SMNb2. Furthermore, it was found that T_c increases slightly (10-20°C) whereas the absolute value of ε_r' decreases with increasing frequency.

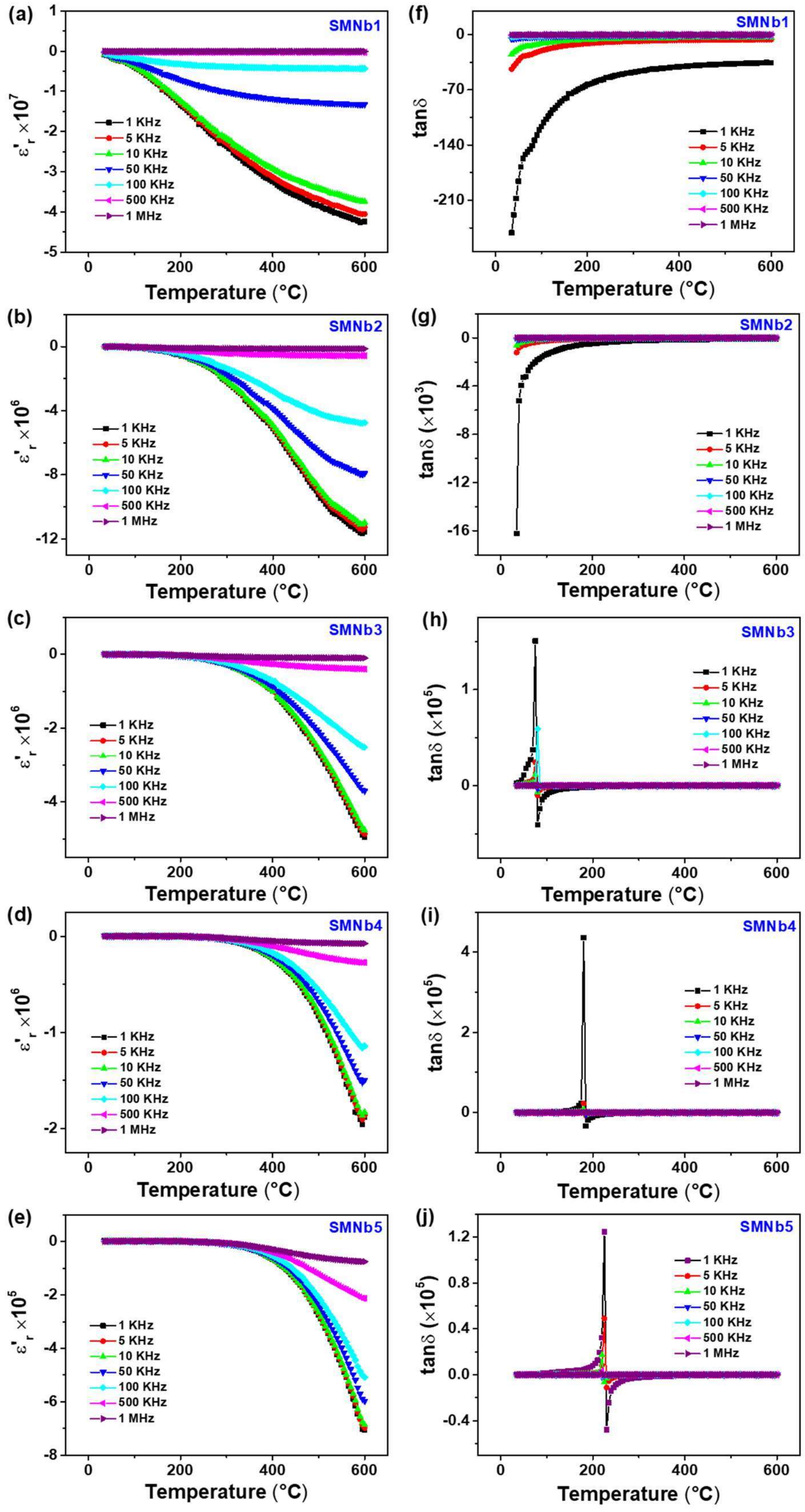

Figure 6.4. Temperature dependence of the real part of the relative permittivity (a-e) and dissipation factor (f-j) at few representative frequencies.

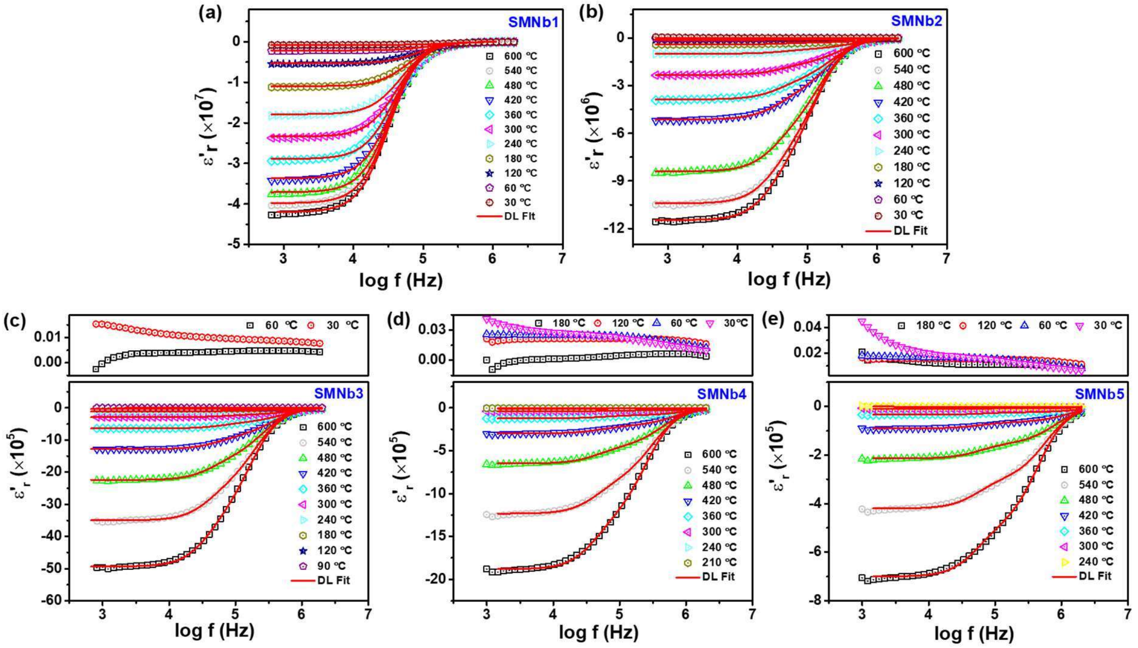

Figure 6.5.Variation of the real part of the relative permittivity with frequency at a few selected temperatures.

To get insight into the origin of negative dielectric constant, the variation ε_r' with frequency at some selected temperatures are shown in Fig. 6.5. As mentioned above, the dielectric constant is negative at all measuring temperatures for samples SMNb1& SMNb2, and for the samples SMNb3, SMNb4 & SMNb5 it remains positive up to a critical temperature (T_c) and becomes negative above this temperature. Therefore, for the samples SMNb3, SMNb4 & SMNb5 the variation of ε_r' with frequency for the measured temperatures was divided into two groups, above T_c and below T_c. The variations of ε_r' with temperature above T_c are shown in the main graph and below T_c are shown in the inset of respective graphs. The main graphs of Fig. 6.5 show the variation of ε_r' with increasing frequency for the temperatures above T_c. In the frequency range 1 kHz to 2 MHz, values of ε_r' remain negative but absolute values decrease with increasing frequency. In general, the plasma-like behavior is responsible for negative permittivity. In 1900 Drude proposed a model to explain the negative permittivity behavior of metals [108,153,229,234]. We tried to fit the Drude model to the experimental data points shown in Fig. 6.5 for all samples. It was observed that experimental data points are not in agreement with data generated according to the Drude model, the reason may be the presence of both bound (localized) and free (delocalized) electrons in the samples. The Drude-Lorentz (DL) model has been employed by the researchers to explain the dielectric response of the materials possessing both localized (bound) and delocalized (free) charge carriers. According to this model, the real part of the complex permittivity (ε_r') is described as follows [236]:

$$\varepsilon_r' = \varepsilon_\infty - \frac{\omega_{pd}^2}{\omega^2 + \tau^{-2}} + \frac{\omega_{pl}^2(\omega_0^2 - \omega^2)}{(\omega_0^2 - \omega^2)^2 + \omega^2\gamma^2} \qquad (6.5)$$

where, ε_∞ is the permittivity extrapolated towards high frequency, ω_{pl} is the Lorentz angular plasma frequency, ω_{pd} is the Drude angular plasma frequency, which is related to carrier concentration (n_{eff}), effective mass (m^*) and, e is a charge of an electron (= 1.6×10^{-19} C)

$$\omega_{pd} = \sqrt{\frac{n_{eff}.e^2}{m^*.\varepsilon_0}} \qquad (6.6)$$

By considering the presence of both free and bound charge carriers in the synthesized samples, we have tried to fit the Drude-Lorentz (DL) to study the dielectric response of all synthesized samples above their critical transition temperature (T_c), which are shown in Fig. 6.5. In these figures, solid lines represent data generated according to the Drude-Lorentz model (Eq. 4) and symbols to the experimental data points. Above critical temperature the ε_r' vs log f curves at different temperatures are in good agreement with the Drude-Lorentz model which confirms the presence of both free and bound charge carriers in all the samples up to the highest temperature of the measurement i.e., up to 600 °C. Absence of resonance characteristics in the experimental data and theoretically calculated data according to Eqn. (6.5) can be attributed to dominating response of plasmonic oscillations of free electrons over the resonance responses of localized charges. Thus, it is clear that the Drude mechanism plays the dominant role in the observed negative permittivity of the samples.

Below T_c, it is observed that the ε_r' values decrease with increasing frequency. A sharp drop in the ε_r' values below 10 kHz are attributable to the interfacial polarization. In addition, the decrease in the ε_r' at a fixed frequency with increasing temperature also supports the presence of interfacial polarization in the SMNb3, SMNb4 & SMNb5 samples. In polycrystalline materials, interfacial polarization arises due to differences in the electrical conductivity of the grains and grain boundaries. In all these three samples a decrease in values of ε_r' with increasing frequency was observed, which is ascribed to the relaxation of space charge polarization. SMNb4 and SMNb5 also consist of impurities of $Sr_8Nb_4O_{18}$ in triclinic phase, and should have different electrical conductivity than tetragonal doped Sr_2MNO_4. This further enhances the interfacial polarization.

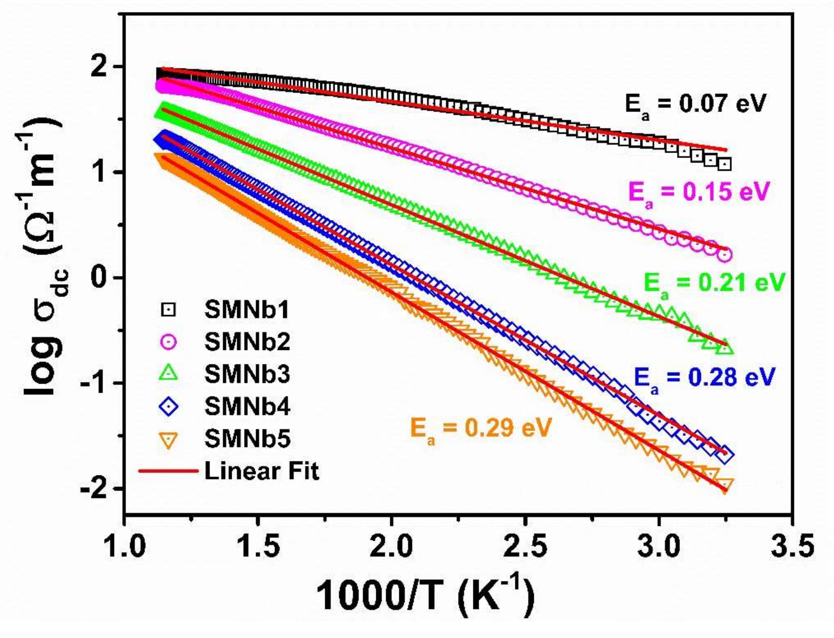

Figure 6.6. Variation of DC conductivity with the inverse of temperature.

The observed negative relative permittivity can be correlated with electrical conductivity. The variation of DC conductivity with temperature for all samples are shown in Fig. 6.6. It is noted from the Fig. 6.6 that the DC conductivity of all the samples increase with increasing temperature and decrease with increasing dopant Nb concentration. The increasing conductivity of samples with temperature ensures the semiconducting nature of the samples even up to 600 °C. The activation energy of DC conduction also increases with increasing Nb concentration. The decrement in electrical conductivity and increasing activation of DC conduction can be explained as follows. In prepared samples Mn and Nb cations are present, and both may exist in a mixed-valence state. The XPS analysis has outlined that the Mn cations are present in both Mn^{3+} and Mn^{4+} states, however, the Nb cations are present only in Nb^{5+} state. Although, the concentration of Mn^{3+} cations decreased with increasing Nb concentration. The Mn^{3+} cation with an electronic configuration of $[Ar]\ 3d\ t_{2g}^3 e_g^1\ 4s^0$ has an additional electron in e_g orbital than Mn^{4+} cation with electronic configuration $[Ar]\ 3d\ t_{2g}^3 e_g^0\ 4s^0$, and Nb^{5+} cation with electronic configuration $[Kr]\ 4d^0\ 5s^0$ has no electron in their outermost orbit. The additional $3d\ e_g$ electrons of Mn^{3+} cations can transfer locally to the higher valence state of Mn^{4+}/Nb^{5+} (present at nearest neighbouring sites), through an oxygen ion and contribute to electrical conduction. The transfer of electrons to the nearest neighbouring Mn^{4+} cations is more probable than Nb^{5+} cations, due to equivalent electronic state of Mn^{4+}. The transfer probability depends upon availability of the equivalent sites (Mn^{4+}) and thermal energy. The increasing Nb concentration in the Sr_2MnO_4 matrix reduces the availability of Mn^{4+} cations in the nearest neighbour sites of Mn^{3+}. Thereby reduces the DC electrical conductivity as well as increasing the DC conduction's activation energy with increasing Nb concentration. The impurity phase ($Sr_8Nb_4O_{18}$) present in SMNb4 and SMNb5 samples may also be responsible in the reduction of DC electrical conductivity and increment in activation energy, due to its insulating nature. Furthermore, the decrement in Mn^{3+} cations concentration with increasing Nb concentration also reduces DC conductivity. The combination of these factors leads to the conductivity of the samples in the order SMNb1 > SMNb2 > SMNb3 > SMNb4 > SMNb5. It is important to mention here that the temperature at which permittivity changes sign, i.e., critical temperature (T_c) is in reverse order of DC conductivity, i.e., T_c of SMNb5 > SMNb4 > SMNb3 > SMNb2 > SMNb1. It means that critical temperature (T_c) is inversely proportional to DC conductivity, σ_{dc}. The DC conductivity, $\sigma_{dc}(= ne\mu$, where n - charge carrier density, e-electronic charge, μ- mobility of the electron) is directly proportional to charge carrier concentration and their mobility, and hence critical transition temperature (T_c) of doped Sr_2MnO_4 can be tuned by chemical doping.

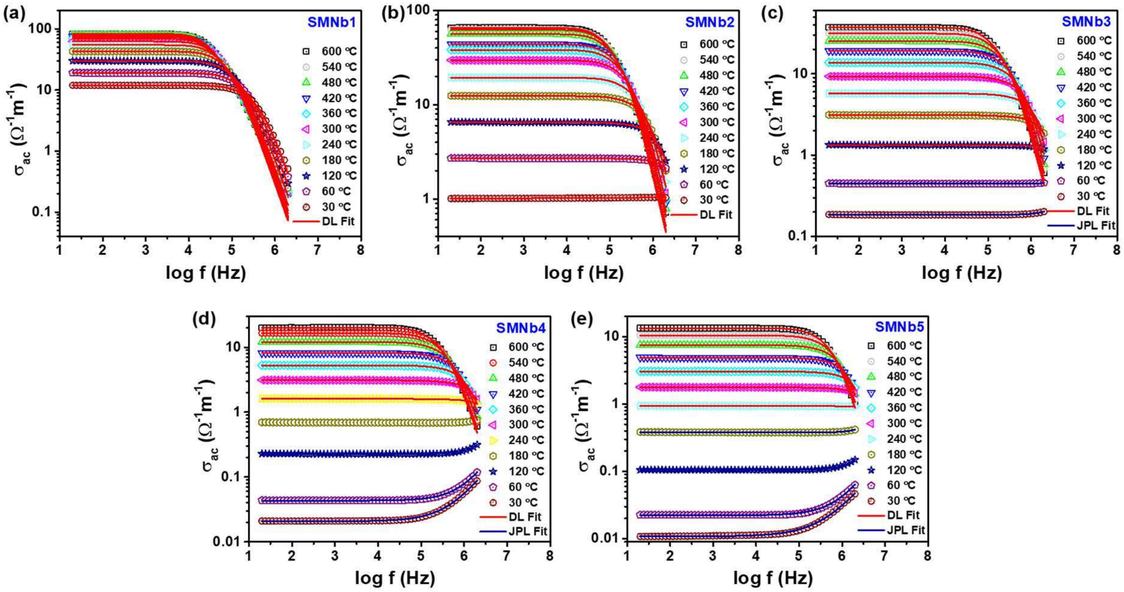

Figure 6.7. AC conductivity spectra of the samples at some representative temperatures.

Fig. 6.7 shows the frequency dependences of ac conductivity at a few temperatures for all the samples. The ac conductivity, σ_{ac} the curve remains constant up to a particular frequency and above that it depends on the frequency. The scattered data points are experimentally measured data points and solid lines represent fitting according to two different theoretical models. It is observed that below critical transition temperature (T_c) σ_{ac} is almost frequency independent up to a particular frequency (called hopping frequency, ω_h) and above this frequency, σ_{ac} increases with the frequency (Fig. 6.7). The incremental part represents the capacitive properties and the $\sigma_{ac} \sim f$ relationship is in accordance with the Jonscher's power law [238]:

$$\sigma_{ac} = \sigma_{dc} + A\omega^n \qquad (6.7)$$

where σ_{dc} is direct conductivity, ω is the angular frequency, A is the pre-exponential factor and n is the frequency exponent that lies between $0 < n < 1$. A good fitting of Jonscher's power law to the conductivity results for the temperatures below the critical temperature (T_c) indicates that the conduction mechanism is dominated by hopping of charge carriers that are localized at defects.

Above critical transition temperature, the decreasing part of the conductivity shows metal-like conduction behavior (skin effect of free electrons) in the samples. The Drude-Lorentz oscillator model was used to account for the high temperature (above T_c) conduction behavior. According to this model, conductivity is related to various parameters as shown in the Eqn. (6.8) [236]:

$$\sigma_{ac} = \frac{\sigma_{dc}}{1 + \omega^2\tau^2} + \frac{\varepsilon_0 \omega_{pl}^2 \omega^2 \gamma}{(\omega_0^2 - \omega^2)^2 + \omega^2\gamma^2} \qquad (6.8)$$

where,σ_{dc} is the dc limit of Drude conductivity, τ is the average scattering time of carriers, ω_{pl} is the Lorentz angular plasma frequency, ω_0 is the resonance frequency, and γ is the damping factor. The first part of the Eqn. (6.8) represents the contribution of free electrons, while the second part to the resonance response of localized/bound electrons. A good matching between measured data points and calculated ones according to Eqn. (6.8), confirm the presence of both free and bound charges in the samples. The change in conduction mechanism with increasing temperature elucidates the dominating role of free charge carriers with increasing temperature. The observed change in the ac conduction mechanism can be explained as follows: at lower temperatures (below T_c) electrons localized at Mn^{3+} contribute to the ac conductivity, σ_{ac} by hopping mechanism [263–265] while at high temperatures (above T_c) electrons localized at Mn^{3+} get delocalized by thermal excitation processes reaching the conduction band and behave as free charge carriers. These free charge carriers will govern the ac conduction mechanism as observed in the metals (skin effect, decrease in the conductivity with increasing frequency according to the Drude model).

6.4 Conclusions

The Nb substituted layered oxides $Sr_2Mn_{1-x}Nb_xO_4$ (x = 0.1, 0.2, 0.3, 0.4, 0.5) were synthesized using the solid-state reaction technique. However, compositions with x = 0.4 and 0.5 consist of an impurity phase $Sr_8Nb_4O_{18}$, and indicates the solubility limit $x < 0.4$ in the lattice of Sr_2MnO_4. The Rietveld refinement confirmed tetragonal structure with space group I4/mmm same as of the Sr_2MnO_4 for the compositions with x = 0.1, 0.2 & 0.3. SEM images have exhibited changes in the grain's morphologies on Nb substitution. XPS analysis indicated the presence of Mn in mixed-valence states Mn^{3+}- Mn^{4+}, whereas Nb in the Nb^{5+} state. Studies of permittivity and AC conductivity with respect to temperature and frequency have shown negative permittivity in the entire range of the measurement (30-600°C) for x = 0.1 and 0.2 compositions, whereas in x = 0.3, 0.4, and 0.5 compositions above 80 °C, 180 °C, and 230 °C, respectively. The plasmonic oscillations of free carriers generated by thermal excitation process(s) are responsible for the observed negative permittivity in the frequency range 1kHz-2 MHz. The presence of both localised and free charge carriers in the samples was confirmed by an excellent match between experimental data ($\varepsilon_r'$and $log\, \sigma_{ac}$ vs $log\, f$ plots) and data derived using the Drude-Lorentz model. Increasing values of DC conductivity with temperature for all the samples confirmed semiconducting nature. Lastly, it is concluded that the temperature at (and above) which negative permittivity is observed in the compositions of the system $Sr_2Mn_{1-x}Nb_xO_4$ is a function of Nb concentration (x). The desired temperature at which negative permittivity appears can be tailored by choosing an optimum Nb concentration, making them promising candidates for switching devices.